RESEARCH ARTICLE

CrossMark

The effect of flow control on the wake dynamics of a rectangular bluff body in ground proximity

H. -J. Schmidt[1] · R. Woszidlo[1] · C. N. Nayeri[1] · C. O. Paschereit[1]

Abstract

The time-resolved flow field in the wake of a rectangular bluff body in ground proximity is examined through wind tunnel experiments. In addition to an extensive assessment of the baseline wake dynamics, the study also investigates the impact of passive (i.e., base flaps) and active (i.e., fluidic oscillators) flow control on the wake dynamics. The velocity field downstream of the model is acquired with a stereoscopic high-speed particle image velocimetry system at several streamwise and crosswise sections. Coherent wake structures are determined by conditional averaging, spectral analysis, and spectral proper orthogonal decomposition. The baseline flow field is dominated by a wake bi-stability that is characterized by a random shift between two stable wake states. The bi-stability is governed by the model's aspect ratio and occurs in the vertical direction, because the model height is 1.35 times larger than its width. Higher frequency modes with less energy content as determined in the appropriate literature are identified and visualized. A coupling between these modes and the bi-stability is discussed. Flow control has a significant impact on the wake dynamics. When passive flow control is applied, the bi-stability of the wake is still present for a flap angle of 20°. The higher frequency modes are still detectable but weakened. The turbulence intensity is significantly reduced when the flow attaches to the base flaps and the bi-stability is inhibited. When active flow control is applied, the higher baseline frequencies are suppressed in addition to the absence of the bi-stability. Solely the dominant mode at a Strouhal number of about 0.08 remains present for all flow control configurations. This mode is attributed to an alternating shear layer oscillation.

1 Introduction

The desire for reducing the aerodynamic drag of bluff bodies has been a driver for numerous research efforts. These scientific endeavors are motivated by the practical relevance of bluff bodies (e.g., for the transportation industry). Several studies initially focused on the detailed description of the natural flow field of bluff bodies. Early studies investigated the mean flow conditions of different geometries (e.g., Mason and Beebe 1978; Ahmed et al. 1984) and their optimization by adding simple devices for passive flow control (e.g., Peterson 1981; Cooper 1985). Modern measurement techniques and advanced computational capabilities

enabled a deeper insight into the turbulent wake that is responsible for the large drag of bluff bodies. Several recent studies focused on the description of transient effects by determining the coherent wake structures and their characteristic frequencies. The frequencies identified in these studies were similar and were attributed mostly to the same spatial flow effects. Duell and George (1999) examined a bus-shaped bluff body model with a square-shaped frontal area. They observed a so-called wake pumping at a normalized frequency of $St_H = fH/U_\infty = 0.069$ (based on the model height H) and a shear layer vortex shedding frequency of $St_H = 1.157$. The low-frequency mode was also determined by other experimental and numerical studies [e.g., by Krajnović and Davidson (2003), Khalighi et al. (2001), Khalighi et al. (2012), or Volpe et al. (2015)] and may be ascribed either to the interaction of the opposite parts of the recirculation vortex (torus) or to a lateral oscillation induced by separated shear layer vortices. Volpe et al. (2015) determined the occurrence of several dominant low-frequency modes by time-resolved pressure measurements at the rear end of an Ahmed model with a blunt rear end. Strouhal

✉ H. -J. Schmidt
hanns-joachim.schmidt@tu-berlin.de

R. Woszidlo
rene.woszidlo@gmail.com

[1] Institute of Fluid Dynamics and Technical Acoustics, Hermann-Föttinger-Institut, Technische Universität Berlin, Berlin 10623, Germany

numbers of $St_H = 0.13$ and 0.17 were associated with the interaction of opposite shear layer vortices separating at the base edges. This shear layer interaction was also observed by Grandemange et al. (2013b). In addition, Volpe et al. (2015) observed a relation between the base pressure and the velocity fluctuations in the mid-section of the upper shear layer at $St_H = 0.08$ indicating the presence of wake pumping as described by Duell and George (1999).

Beside these wake modes, the natural wake of a box-shaped, bluff body is mostly dominated by a random switching motion between two preferred states. The bistable behavior of the recirculation area is characterized by a shift from one asymmetric state to the other after a random dwelling time. Grandemange et al. (2013b) estimate that the time which the wake stays in one preferred position scales with $10^3 H/U_\infty$ which is three orders of magnitude higher than typical wake timescales. Both asymmetric wake orientations occur statistically with the same probability. The asymmetric wake induces a transient lateral force in the respective direction. The spatial and temporal behaviors of these long-time dynamics and the boundary conditions at which they occur were examined on square-back models similar to the Ahmed body [e.g., by Grandemange et al. (2013b), Volpe et al. (2015), Evrard et al. (2016)] and on the Windsor model [e.g., by Perry et al. (2016), Pavia et al. (2017)]. In these studies, the preferred direction of the bistable shift motion is in the lateral direction when a critical ground distance of $z/H = 0.1$ is exceeded. However, Cadot et al. (2015) determined that the wake stability bifurcation depends not only on the ground clearance, but also the Reynolds number. The ground clearance to achieve bi-stability decreases with increasing Re. Then, the stability persists for different geometric configurations (Grandemange et al. 2013a). In addition, Grandemange et al. (2013a) obtained a bi-modal behavior in the vertical direction for an inverse aspect ratio ($H/W = 1.34$), which occurs particularly at a ground clearance of $d/H \approx 0.1$. Unlike the horizontal bi-stability, the vertical modes are not symmetric due to the presence of the ground.

The bistable shifting motion has not been found in all studies on bluff bodies (e.g., Krajnović and Davidson 2003; Barros et al. 2016b). Therefore, further studies focus on the control of the horizontal transition between the preferred states by adding additional perturbations. The influence of small control cylinders on the bi-stability and the resulting forces are discussed by Grandemange et al. (2014). Depending on the location of the perturbation, the bi-stability is unaffected or suppressed, or remains at one stable position. The authors assessed the pressure drag increase induced by the bi-stability to 4–9%. Different underbody perturbations with variable dimensions are investigated by Barros et al. (2017) on the same model. The lateral bi-stability occurs for intermediate size perturbations; otherwise, vertically

asymmetric states occur. This study provides some suggestions for the influence of the mounting on the wake's dominant bistable shifting motion. In summary, the previous studies have extensively examined the bi-stability regarding its characteristic timescales, the spatial alignment, as well as the effect of geometric boundary conditions or perturbations. The energy content of the bi-stability is one order of magnitude higher than the higher frequency modes. To the author's knowledge, a connection between the wake's bi-stability and the higher frequency modes has not been discussed in detail in the literature so far. Only Pavia et al. (2017) determine a link between the bistable motion and the wake pumping.

Rear-end modifications such as base flaps are effective devices for the drag reduction of bluff bodies and their influence on the wake dynamics is reported in several studies. Duell and George (1999) observed a suppression of the bubble pumping mode and a base pressure increase of 11% at a cavity depth of $0.8\ l_{flap}/H$, where l_{flap} is the flap length. This change of pressure drag may be attributed to the downstream postponement of the turbulent wake modes. Khalighi et al. (2001) exhibited a drag reduction of 20% when adding a base cavity with $0.5H$ that reduces the turbulence intensity by approximately 10% accompanied by a suppression of the fluctuations at $St_H \approx 0.07$. The numerical investigation of an Ahmed body by Lucas et al. (2017) indicates the suppression of the bistable wake motion by the presence of a base cavity which resulted in a decrease in pressure-induced drag. Khalighi et al. (2012) determined a damping of the $St_H = 0.08$ and $St_H = 0.18$ modes for a boat tail with the same length accompanied with a significantly drag reduction of 30%. Evrard et al. (2016) investigated the effect of the base cavity length on the long-time dynamics reported by Grandemange et al. (2013b). The footprint of the bi-stability was clearly detectable by the base pressure distribution and decreases with increasing cavity size. In general, a stabilization of the wake and a distinct mean base pressure increase occurs when the normalized cavity length exceeds $l_{flap} = 0.24H$. The sensitivity of the bi-stability to horizontal trailing edge chamfers is investigated by Perry et al. (2016). The wake tends to a single symmetric, less turbulent state as long as the shear layers are deflected inward.

The prevailing vortex structures of the bistable states are reconstructed by several authors. Evrard et al. (2016) assume an alteration of the mean vortex system from the bistable pair of randomly occurring mirrored modes to a less energetic, static, torus-shaped vortex as described by Krajnović and Davidson (2003). Both time-averaged vortex systems are visualized based on conditional averaging. A pair of curved, counter-rotating, streamwise vortices connected to the close wall recirculating vortex forms a horseshoe-shaped vortical structure. Perry et al. (2016) hypothesize that the lateral vortex close to the base forms an isolated transversal vortex, whereas a C-shaped streamwise vortex occurs instead

of the horseshoe vortex assumed by Evrard et al. (2016). Pavia et al. (2017) extensively investigated the topology of the wake's bi-stability downstream of a Windsor body. A vertical hairpin vortex is proposed that originates at one trailing edge bending over to the other side while shifting downstream, which is similar to the topology assumed by Evrard et al. (2016). Farther downstream, both parts merge to a single streamwise vortex.

Beyond these geometric (passive) modifications, active flow control (AFC) represents a more invasive procedure to provide an effective flow field manipulation due to the additional energy input at desired locations. Over the recent decades, a variety of AFC methods have been investigated at various two- or three-dimensional models to determine the most efficient flow control method. As a subcategory of bluff bodies, several efforts have been focused on the AHMED reference body. Brackston et al. (2016) developed a feedback controller that successfully suppresses the wake's bi-stability using oscillating flaps at the rear end. A drag reduction of 2% was measured for the controlled wake. Khalighi et al. (2012) numerically investigated the effect of COANDA blowing on the wake dynamics. They achieved a drag reduction of up to 50% for a jet velocity twice the freestream velocity, which agrees to the experimental results of Englar (2001). A wide portion of the flow field remains nearly unaffected by any measurable dominant mode. The spectra extracted from selected positions within the velocity field exhibit a damping over the entire frequency band.

These publications indicate a direct relation between base pressure and wake dynamics, which may be summarized in simple terms: the energy content of the wake modes correlates with the pressure drag.

Therefore, Barros et al. (2014) focus on the direct manipulation of a global wake mode via low- and high-frequency pulsed jets which exit tangentially to the model's side faces. The low-frequency actuation at $St_H = 0.4$ amplifies the wake modes by enhancing the shear layer roll-up that increases the entrainment and, therefore, reduces the wake size. In addition, Barros et al. (2016a) exhibit an amplification of the shedding frequency by periodic forcing which yield a resonance effects within the wake. As a consequence, a significant decrease of the base pressure is obtained. The high-frequency actuation ($St_H = 11.5$) causes a dampening of the wake modes and a decrease of the pressure drag by $\Delta C_D \approx 10\%$. The relevance of the shear layer for the entire wake dynamics and its sensitivity to manipulations was determined.

Barros et al. (2016b) extended these investigations to yield a distinct reduction of the turbulent energy in the wake when employing high-frequency actuation. Whereas the low-frequency actuation enhances the shear layer roll-up to entrain more 'external' momentum into the wake which increase the overall turbulence intensity, the high-frequency

actuation deflects the shear layer farther inwards, significantly reduces its growth rate, and reduces the entrainment of external momentum. Li et al. (2016) used feedback-controlled lateral jets to inhibit the bi-modal shifting motion. One-sided actuation forced an asymmetric state independent of the actuation frequency resulting in a base pressure decrease of 10%, whereas the feedback control with a forcing frequency of $St_H = 0.8$ yields a symmetric wake and a base pressure recovery of 2%. Barros et al. (2016b) achieved a decrease in base pressure by 12% at an actuation frequency of $St_H = 0.8$ which is attributed to the enhanced shear layer cross-flow dynamics. These outcome explain the moderate drag reduction of Li et al. (2016).

The current paper focuses on the unsteady flow effects past a bluff body model with an aspect ratio of $H/W = 1.35$ in ground proximity with and without active flow control. The characterization of the dominant wake modes is further pursued to obtain information about their spatial occurrence and orientation. The bi-stability is investigated and its connection to the higher frequency modes is described. Base flaps as passive and fluidic oscillators as active flow control are applied to the model and assessed with regards to the emerging wake dynamics. Fluidic oscillators generate a self-sustained, high-frequency oscillating jet at the outlet without the use of moving parts. The oscillator's governing internal dynamics and the external flow field ejected into a quiescent environment is provided by Woszidlo et al. (2015). Schmidt et al. (2015) discussed the global effect of these passive and active flow control approaches on the same model without any detailed study of the wake dynamics.

2 Experimental setup and instrumentation

The bluff body model experimentally investigated in the current study corresponds to the GETS (General European Transport System) geometry introduced by Van Raemdonck and Van Tooren (2008). It was developed as a simplified representation of a European long-haul, heavy-duty vehicle without any of its geometric details (e.g., tires, side mirrors, gap between truck and trailer, etc.). The model's rectangular shape has a height-to-width ratio of $H/W = 1.35$ that is similar to the inverse aspect ratio of an AHMED body. In addition, a rounded front is attached to the model with a radius of 54 mm ($0.15H$) to overcome the critical REYNOLDS number as determined by Cooper (1985). The front is equipped with turbulence tapes to suppress laminar separation. The model, its air supply system, and the internal retaining structure are illustrated in Fig. 1a. The top and side faces are made from aluminum plates, which are attached to the inner structure that is connected to the external balance underneath the test section via vertical struts. Gaps between these plates and screw holes are sealed with modeling clay. The outer
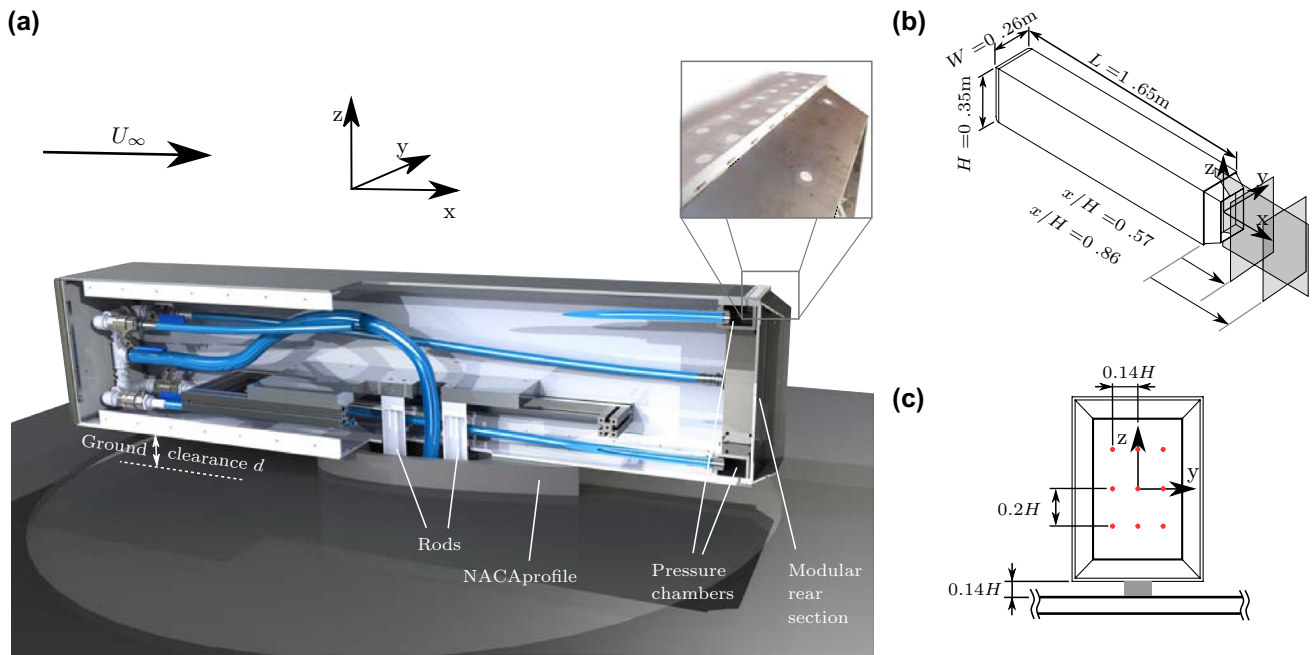
(a)

(b)

(c)

Fig. 1 Illustration of the GETS model: **a** visualization of the model mounted in the wind tunnel including the hose system for the actuation and the detailed visualization of the rear end components (small window), **b** a schematic illustration of the model's dimensions including the position of the PIV measurement sections, and **c** the location of the base pressure taps

dimensions of the model are visualized in Fig. 1b. The origin of the coordinate system referred to in this work is located at the center of the model's base plate (Fig. 1b, c). Base flaps are attached to the model's rear end with a slight inward shift to ensue enough space for the oscillator nozzles (Fig. 1a, small frame). The flap angles, which were chosen according to the results of Schmidt et al. (2015), are listed in Table 3. The flap length is set to $l_{flap}/H = 0.29$ for the current study.

The oscillators are implemented into the rear edges of the model with an inward offset of 4.6 mm (i.e., 1.3% model height H) that is due to manufacturing requirements. The oscillators are milled into small rear-end side-plates to emit spatially oscillating jets parallel to the model's side faces. The equidistant spacing of $\Delta s = 36$ mm between adjacent oscillators is defined on the basis of the results by Schmidt et al. (2015). The external nozzles of the oscillators have a hydraulic diameter of 1.3 mm (0.37% H). The air supply is provided by four pressure chambers located internally behind the base plate. The even distribution of mass flow along the oscillator strips is verified by analyzing the oscillation frequency of each oscillator. Additional information about the implementation of the AFC system and the used oscillator are provided by Schmidt et al. (2015). The thrust generated by the jets is defined by the momentum coefficient $C_\mu = 2A_{jet}/(H \cdot W) \cdot (U_{jet}/U_\infty)^2$. The jet area A_{jet} represents the total exit area of all oscillators combined. Hotwire measurements downstream of the model's orifices determined oscillation frequencies

of $f_{osc} \approx 0.85$ kHz ($St_H = 17.0$) and $f_{osc} \approx 1.22$ kHz ($St_H = 24.4$) for $C_\mu = 1.0\%$ and $C_\mu = 2.5\%$, respectively. Woszidlo and Wygnanski (2011) argue that the effectiveness of the jets does not depend on the sweeping frequency at those considerably high oscillation frequencies. The jet velocity is estimated as bulk velocity at the exit based on the measured mass flow rate and ambient conditions (Schmidt et al. 2015). These velocities are calculated to be $U_{jet} = 3.1U_\infty$ and $U_{jet} = 4.9U_\infty$ for $C_\mu = 1.0\%$ and $C_\mu = 2.5\%$, respectively.

The experiments are carried out in the closed-loop wind tunnel of the Hermann–Föttinger-Institut at the Technische Universität Berlin. The test section has an overall length of 5 m with a cross-section of 2 m × 1.4 m. The freestream velocity is determined via a PITOT-static tube downstream of the wind tunnel contraction at the ceiling of the first test section. The dynamic pressure is measured with a 1000 Pa MKS Baratron *220D* with an accuracy of 0.15%. The maximum applicable freestream velocity in the test section is $U_\infty = 60$ m/s. The experiments are conducted at a freestream velocity of $U_\infty = 35$ m/s which corresponds to a REYNOLDS number of $Re = 6.7 \cdot 10^5$. The ground distance of the model d can be incrementally changed by adapter plates for the vertical rods and the NACA-shaped mounting skirt. In this study, the distance between the model and the splitter plate is set to 0.14H. This ground plate is mounted 0.16 m above the wind tunnel floor to minimize freestream boundary layer effects. The blockage within the test section is less than 10%.

The flow field dynamics of the bluff body are assessed by force, pressure, and laser-based velocity field measurements. The aerodynamic forces are captured by an external six-component balance with a temporal resolution of 2 Hz and an accuracy of 0.3% full scale. The mean drag values are reported as a reference for the description of the general effect of the flow control methods. Two vertical rods for the connection between model and balance, the main air supply hose, and the cables of the pressure sensors are guided through an airfoil mounted to the wind tunnel floor to prevent any distortion of the force measurements and to reduce the freestream perturbations underneath the model. The differential pressure sensors (*HDO Series* by Sensortechnics) with a nominal load of ± 1000 Pa and a maximum error of less than 0.5% full scale are attached to the model's rear base plate to determine the time-resolved static pressure distribution. The pressure data are recorded at a sampling rate of 65 kHz for 25 s. The static pressure provided by the PITOT tube is utilized as the reference pressure. The response time of the sensors is less than 0.1 ms. The pressure taps over the model's base are arranged as an equidistant 3×3 array (Fig. 1c). The sensors are located within the model behind the base plate to keep the distance to the pressure taps as short as possible.

A high-speed stereo PIV system is used to capture the time-resolved velocity field downstream of the model. The measurement system includes a double-pulsed Quantronix *Darwin Duo 100 /Nd:YLF* Laser with an energy output of 60 mJ per pulse and a wave length of 527 nm, a mirror arm, laser sheet optics, and two Photron *Fastcams SA1.1* cameras with a CMOS-Chip resolution of 1024×1024 pixel. A maximum frame rate of 5kHz is possible with this system. The cameras are equipped with Canon *EF 85mm f/1.2 II USM* objectives that are computer-controlled via an EOS ring. The acquired fields of view relative to the bluff body geometry are visualized in Fig. 1b. The cameras are positioned outside the wind tunnel downstream of the model at both sides of the test section to accomplish view angles of approximately 45° relative to the light sheet. The tilt angles are manually adjusted. Atomized silicon oil (DEHS) with an average diameter of 1 μm is used as tracing material. For each test case, a total of 5500 double pictures are recorded with each camera at a frame rate of 500 Hz, which may provide an adequate measurement period for the determination of transient effects. However, the limited measurement time of 11 s may not be sufficient for statistical convergence.

The commercial software PIVview3C v.3.6 is used to calculate the velocity fields. The interrogation window size for the correlations is incrementally reduced via multi-grid interrogation, refining the windows size from the coarse pass of 96 pixels to the final pass with a sample size of 24 pixels. A window overlap of 50% is employed to increase the spatial resolution to approximately 3.6 mm (1.0%H). An outlier detection filter is applied on both vector fields. A residual filter is applied to the three-components (3C) vector reconstruction. Residuals larger than 2 pixels (approximately 2.1% of all vectors) are removed and replaced with the DCT-PLS method as described in Sect. 3.1.

3 Data processing

The time-resolved velocity field data are analyzed in detail regarding coherent wake structures, and their spatial and temporal characteristics. Therefore, missing and significantly deviating vectors are replaced using a PIV filter (Sect. 3.1). The data analysis techniques to determine spatial and temporal information from the velocity data are described in Sects. 3.2 and 3.3.

3.1 Data smoothing

The utilization of the 3C residual filter on the vector reconstruction of the stereoscopic PIV data yields incomplete velocity data (about 2% missing vectors). The computation of frequency spectra at a certain location requires continuous timeseries. Therefore, outliers and missing velocity data are replaced and interpolated via the Discrete Cosine Transform (DCT)-based penalized least-squares (PLS) approach. This algorithm is introduced by Garcia (2011) as a fast and robust filter especially for n-dimensional PIV data. The Matlab function *smoothn* [supplemental material provided by Garcia (2011)] is applied to the entire PIV data set. The smoothing is applied on each snapshot to recover spatial information without smoothing in time. Figure 2a–c visualizes the effect of the *smoothn* filter applied to an arbitrarily chosen PIV snapshot. Figure 2d illustrates the timeseries of the velocity fluctuations at a randomly chosen point S at $(x_S/H, z_S/H) = (0.5, -0.1)$. The power spectral density of both signals is shown in Fig. 2e in terms of the STROUHAL number $St = fH/U_\infty$ where f is the frequency. The missing values of the raw signal are linearly interpolated for that calculation.

The filter has a minor influence on the entire frequency band; especially, it is negligible for the low-frequency band ($St < 1.0$), because the dominant frequencies and their amplitudes do not change significantly. The amplitudes of the high-frequency band ($St \geq 1.0$) are mostly dampened by the filter.

3.2 Spatial frequency and amplitude detection

The temporal behavior of the entire velocity field is analyzed by frequency analysis for each spatial location. Therefore, the power spectra density (PSD) is estimated by the WELCH method to determine the frequency-related power ($P(f)$) of

Fig. 2 Effect of the smoothing on the velocity field: Instantaneous PIV snapshot: **a** raw data, **b** filtered data, and **c** the difference. The effect of the filter is illustrated in terms of: **d** the timeseries of u'_S and **e** the respective frequency spectra P_S at $(x_S/H, z_S/H) = (0.5, -0.1)$
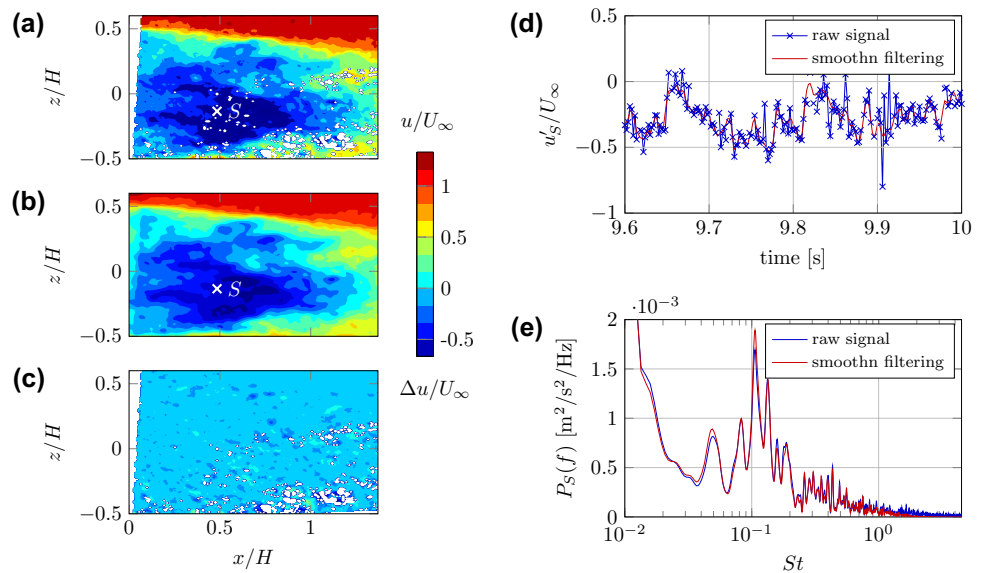
the velocity fluctuations $\boldsymbol{u}'(\boldsymbol{x}, t) = \boldsymbol{u}(\boldsymbol{x}, t) - \overline{\boldsymbol{u}}(\boldsymbol{x})$. The measurement signals are divided into 30% overlapping sequences. Each sequence is multiplied with a HAMMING window. The calculated periodograms are finally averaged to obtain the WELCH estimate of the PSD. The averaging of the modified periodograms significantly reduces the noise of the resulting spectrum, which reduces the influence of large-scale stochastic fluctuations. However, the resolution in frequency is also reduced. In this study, the resolution is $df = 0.06$ Hz which is attributed to zero padding of the measurement signals yielding a finer interpolation of the frequencies.

3.3 Spectral POD

The spectral proper orthogonal decomposition (SPOD) is utilized for the identification of coherent wake structures. This method was developed by Sieber et al. (2016b) to obtain spatial and temporal information on coherent structures, especially within turbulent flows. Unlike the conventional snapshot-POD, time-resolved data are required for the utilization of this method. Following the nomenclature of Sieber et al. (2016b), the velocity fluctuations are decomposed into temporal coefficients a_i and spatial modes $\boldsymbol{\Phi}_i$:

$$\boldsymbol{u}'(t) = \sum_{i=0}^{N} a_i(t)\boldsymbol{\Phi}_i(\boldsymbol{x}) . \tag{1}$$

The temporal correlation matrix $\boldsymbol{R}$ of the data set (normalized with the number of snapshots N) is defined as:

$$R_{i,j} = \frac{1}{N} \int_V \boldsymbol{u}'(\boldsymbol{x}, t_i)\boldsymbol{u}'^T(\boldsymbol{x}, t_j)\mathrm{d}V , \tag{2}$$

where V constitutes the spatial integration region and the operator $()^T$ represents the vector transpose. The temporal coefficients $\mathbf{a}_i$ and mode energies λ_i are computed from the correlation matrix via eigenvalue decomposition:

$$\boldsymbol{R}\boldsymbol{a}_i = \lambda_i\boldsymbol{a}_i \text{ with } \lambda_1 \geq \lambda_2 \geq \cdots \geq \lambda_N \geq 0 . \tag{3}$$

Finally, the spatial modes $\boldsymbol{\Phi}_n(\boldsymbol{x})$ are derived from the projection:

$$\boldsymbol{\Phi}_i(\boldsymbol{x}) = \frac{1}{N\lambda_i} \sum_{j=1}^{N} a_i(t_j)\boldsymbol{u}(\boldsymbol{x}, t_j) . \tag{4}$$

The procedure of the SPOD is similar to the conventional snapshot-POD as outlined in Eqs. 1–4. Sieber et al. (2016b) modify the POD algorithm by applying a low-pass filter on the diagonals of the correlation matrix $\boldsymbol{R}$, to determine the filtered correlation matrix $\boldsymbol{S}$:

$$S_{i,j} = \sum_{k=-N_f}^{N_f} g_k R_{i+k,j+k}. \tag{5}$$

The diagonal elements of $\boldsymbol{S}$ are smoothed by a symmetric, finite impulse response Gaussian filter $\boldsymbol{g}$. The filter width N_f represents a spectral limitation of the SPOD modes. This modification generally provides a better separation of single flow structures, and enables the detection of dynamic effects weaker than both the noise-level and short-term effects (Sieber et al. 2016b). The filter width N_f is defined as an equivalent of the wake pumping period of $St_1 = f_1 H/U_\infty \approx 0.08$ to $N_f = 2fs/f_1 = 250$, where f_s represents the acquisition frequency (Sieber et al. 2016a). The correlation matrix $\boldsymbol{S}$ can be used in Eq. 3 instead of $\boldsymbol{R}$. The calculation of the temporal coefficients and energy content of the modes corresponds to

the aforementioned standard POD algorithm. Sieber et al. (2016b) additionally introduce a method for the determination of coupled modes via the spectral coherence of the temporal coefficients. The relative energy K of a mode pair is the sum of their eigenvalues normalized with the sum of all eigenvalues. The most energetic coupled SPOD modes are phase-averaged in Sect. 4.1.3 for the baseline configuration and in Sect. 4.3 for the AFC cases.

4 Results

The results of the experimental investigations are described in this section . First, the transient effects of the baseline flow field (without passive and active flow control) are illustrated in Sect. 4.1. The general effects of the passive and active flow control approaches are described in Sect. 4.2. Finally, the influence of the flow control on the dominant wake modes is presented in Sect. 4.3.

4.1 The baseline flow dynamics

This section presents the natural flow conditions downstream the GETS model. First, the bi-stability is discussed in Sect. 4.1.1. The higher frequency modes are described in Sect. 4.1.2. Finally, the SPOD is applied to the baseline velocity data to give an overview on the spatial emergence of the most dominant modes and their connection to the bi-stability (Sect. 4.1.3).

4.1.1 The bi-stability of the wake

Figure 3a illustrates the baseline flow field in terms of the distribution of the normalized covariance of the in-plane velocity fluctuations $\overline{u'w'}/U_\infty$. In addition, the size of the recirculation area is marked, which is determined as the region in which the streamwise velocity component is negative ($\overline{u} < 0$). Typical areas of large REYNOLDS stresses $\overline{u'w'}/U_\infty$ are the shear layers and the center of the

recirculation vortices. The shear layer vortices transfer higher momentum from the freestream into the wake. The presence of the ground reduces the intensity of the lower shear layer. However, the underbody flow provides enough momentum to maintain the typical, organized bluff body wake structure as reported in the literature [e.g., by Duell and George 1999; Krajnović and Davidson 2003]. The inner wake dynamics are governed by the interaction between the vortex separation from the base edges and the dynamic of the free stagnation point (S4 in Fig. 3a). Figure 3b visualizes the timeseries of the streamwise velocity fluctuation u' extracted at the locations $S1$ and $S2$ which mark the center of the recirculation vortices. The extracted timeseries reveals that the flow shifts randomly between two stable equilibrium states, which indicates a bistable wake behavior. The streamwise velocity fluctuations at $S1$ and $S2$ are in anti-phase. The related frequency spectra are shown in Fig. 3c. Beside the typical wake frequencies, the most power is related to the low-frequency bi-stability ($St \approx 0$).

A footprint of the bistable wake motion is extracted from the base plate pressure values. Figure 4a visualizes the evolution of the pressure coefficients located in the vertical mid-plane as a function of time. The related probability distributions show two distinct peaks, which emphasize the random shift between the two stable positions as determined from the velocity data. The asymmetry of the probability distributions is attributed to the limited time of measurement and becomes statistically symmetric. The pressure gradient along the base plate is calculated for the identification of the orientation bistable wake and illustrated in Fig. 4b in terms of the vertical ($C_{P_{8,2}}$) and the horizontal ($C_{P_{6,4}}$) base pressure gradient. The vertical pressure gradient exhibits the characteristic shift that is consistent with the timeseries of the pressure coefficients in Fig. 4a and the velocity fluctuations of Fig. 3b. The horizontal pressure gradient $C_{P_{6,4}}$ remains nearly constant over the entire measurement period, which confirms the vertical orientation of the bi-stability.

In general, these outcomes are consistent with the results of Grandemange et al. (2013a). The ground clearance is
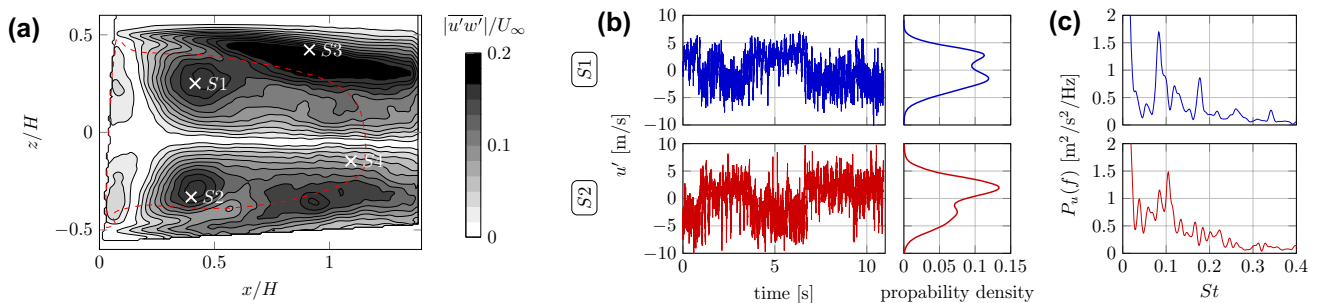

Fig. 3 **a** Distribution of REYNOLDS shear stresses within the flow field; the red dashed line indicates the region of the recirculation ($\overline{\mathbf{u}} < 0\,m/s$), **b** timeseries and probability distributions at position S1 and S2, and **c** respective frequency spectra
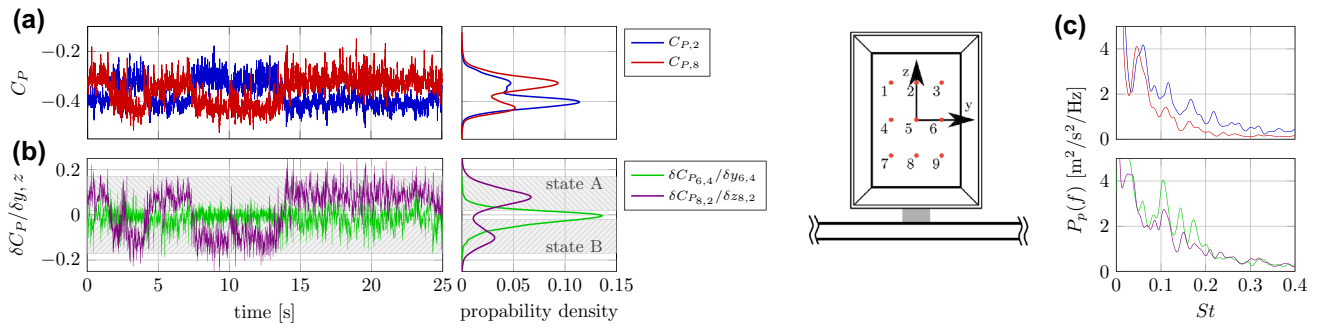
Fig. 4 Time evolution and probability distributions of **a** the pressure signals at tap positions 2 and 8, **b** the vertical and horizontal pressure gradient, and **c** the frequency spectra of the respective base pressure values

large enough to provide enough momentum to suppress flow separation at the ground and to form the characteristic shape of the near-wake region illustrated by Duell and George (1999). Based on the current results, the preferred orientation of the bi-stability appears to be governed by the model's aspect ratio and, therefore, occurs in the vertical direction in this study.

Conditional averaging based on the vertical pressure gradient $\delta C_P / \delta z$ is applied to the PIV data. The snapshots are sorted and averaged regarding the sign of the vertical pressure gradient within the range of $0.02 \leq |\delta C_P / \delta z| \leq 0.17$ (highlighted with gray bars in Fig. 4b).

The resulting vertical streamwise velocity fields are visualized in Fig. 5a, b. The conditionally averaged velocity fields deviate from the mean velocity field by an alternating

dominance of the recirculation vortices and the vertical shift of the free stagnation point. The respective dominant vortex close to the model's rear end induces the low pressure footprint determined in Fig. 4a. In addition, the velocity data obtained from the cross sections $x/H = 0.57$ and $x/H = 0.86$ are conditionally averaged with reference to the vertical pressure gradient (Fig. 5c, d). State A is selected for the averaging process, because it is over-presented during the sampling time of the measurements. A pair of counter-rotating streamwise vortices is detected at the upper part of the velocity field of Fig. 5c, which convects farther downstream while shifting downwards (Fig. 5d). The downward deflection of the counter-rotating vortices is induced by the dominant part of the recirculation vortex identified in Fig. 5a. These vortices form a curved horseshoe-shaped
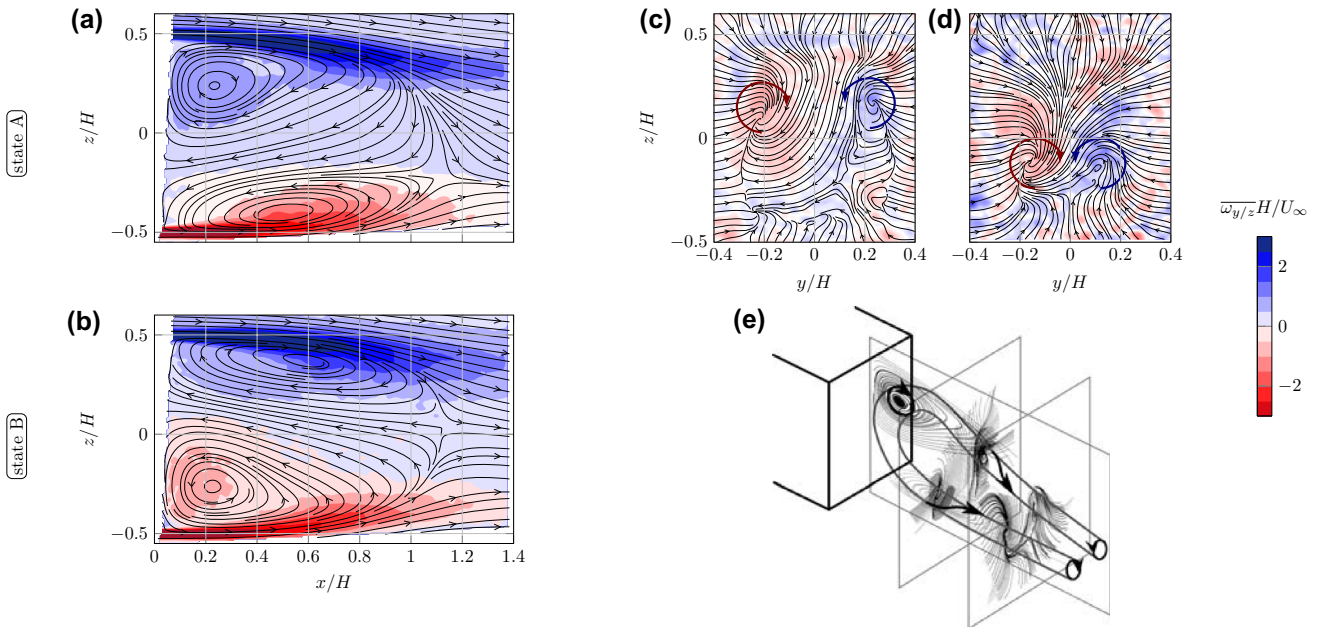

Fig. 5 Conditionally averaged flow fields: Distribution of vorticity at **a** state A and **b** state B in the streamwise direction; and for state A the cross sections at: **c** $x/H = 0.57$ and **d** $x/H = 0.86$ downstream the rear plate. The main vortex formation of state A is illustrated in **e**

Table 1 Dominant frequencies extracted at characteristic locations within the wake (marked in Fig. 3a)

Position	St_u	St_w	St_v
S1	0.08, 0.18	0.08, 0.18	
S2	0.11	0.18, 0.22	0.18
S3	0.22, 0.30	0.18, 0.22, 0.28	0.22
S4	0.05, 0.18	0.18, 0.27	

vortex structure. This dominant vortex system is reconstructed for state A in Fig. 5e. The obtained flow field agrees well with the observations of Evrard et al. (2016).

4.1.2 Determination of the dominant modes

The frequency spectra illustrated in Figs. 3c and 4c indicate the presence of frequencies typically determined downstream of a bluff body. Wake modes as reported in the literature (e.g., vortex shedding at $St_H = 0.18$) are evident with minor deviations in the frequency which are likely attributed to the different model shape and boundary conditions. The height of the GETS model H is defined as the geometric reference length and characteristic length scale for dimensionless quantities, and hence, the STROUHAL number is defined as $St_H = f \cdot H/U_\infty = St$. To reduce the dominance of the bi-stability for the spectral analysis, a second-order BUTTERWORTH high-pass filter with a cut-off frequency of 2 Hz is applied to the data for further frequency analysis.

Table 1 illustrates the most dominant frequencies extracted from the frequency spectra computed at locations marked in Fig. 3a. The selected locations represent the upper and lower cores of the recirculation torus (S1 and S2, respectively), an arbitrarily chosen location in the shear layer S3, and the free stagnation point S4. The extracted dominant

frequencies are similar to the values reported in literature. In addition, a STROUHAL number of about $St = 0.28 - 0.3$ is found within the shear layers.

Table 2 summarizes the general effects as classified in the literature, the related normalized frequencies, and the spatial distribution of power in the streamwise direction P_u and vertical direction P_w. Shear layer modes cover a wide range of frequencies. The St_3 mode is the most prominent in the current data set, which motivates further investigations on that mode. The spatial distribution of P_u and P_w provides general information on the location and orientation of the respective phenomena. The bi-stability ($St \approx 0$) affects large coherent areas, whereas the higher frequency modes dominate smaller isolated regions. Khalighi et al. (2001) assign the STROUHAL number of $St_1 = 0.08$ either to the alternating vortex shedding or to the wake pumping that is attributed to the vortex isolation and downwash from the free stagnation point. Larger amplitudes are determined specifically at the upper shear layer, and smaller amplitudes within the recirculation area and at the free stagnation point. A distinct orientation cannot be determined in these regions. The St_2 mode represents another frequency that is commonly allocated to the interaction of the alternating vortex shedding at the opposite rear edges. This effect becomes evident farther downstream as reported by Khalighi et al. (2001). The St_3 mode also represents a shear layer mode near the free stagnation point which mainly oscillates in vertical direction.

Figure 6 visualizes the power spectra computed along the vertical planes at $x/H = 0.31, 0.74$, and 1.0. Apart from the St_1 mode, the streamwise fluctuations of the dominant modes occur predominantly within the shear layers with increasing vertical extent when convecting downstream, whereas the vertical fluctuations are located within the center of the wake. The increased exchange of momentum from one velocity component to the other is attributed to the dominant

Table 2 Classification of the most dominant wake effects, their characteristic frequencies, and the spatial occurrence in the vertical and streamwise direction in the range: $0 \leq x/H \leq 1.4$ and $-0.55 \leq x/H \leq 0.55$ (yellow color indicates larger amplitudes)

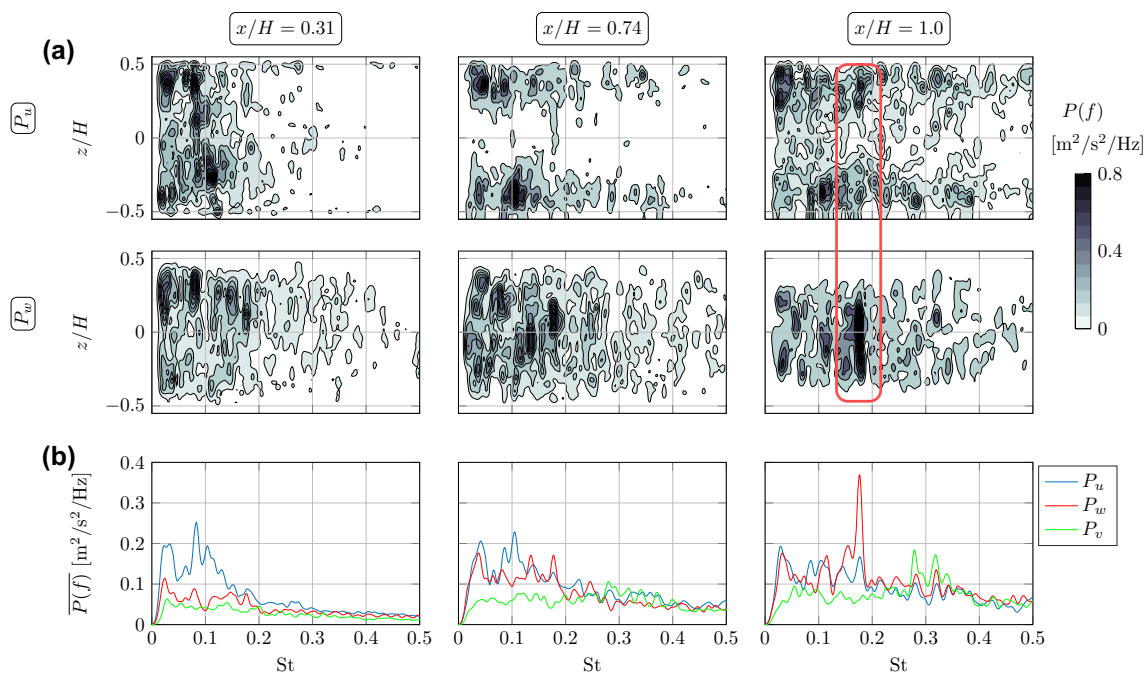| Terminology	STROUHAL number	Spatial amplitude distribution	
		P_u	P_w
Bi-stability	$St_0 = 0$		
Wake pumping	$St_1 = 0.08$		
Vortex shedding	$St_2 = 0.18$		
Shear layer roll-up	$St_3 = 0.28$		

Fig. 6 Frequency spectra at different streamwise positions. Visualization of: **a** spectral content along the vertical direction and **b** power spectral density integrated along the z-coordinates

vortices within the shear layers and the recirculation area, which are regions of high REYNOLDS stresses (Fig. 3). An example of the transition of the velocity fluctuations in regions of large REYNOLDS shear stresses $\overline{u'w'}$ is marked in Fig. 6. The St_1 mode is evident in the streamwise and vertical direction over the entire wake with decreasing intensity farther downstream, which indicates that the origin of this mode is located within the shear layers. Khalighi et al. (2012) determined a growth of the St_2 mode with increasing distance to the model, which appears as vertical oscillations within the shear layers and manifests as intense vertical fluctuations near the free stagnation point. The frequency fields of Fig. 6a are averaged along the respective z-coordinate in Fig. 6b to visualize the dominant frequencies in these cross sections. Beside the aforementioned dominant frequencies, another dominant frequency at $St = 0.13$ is detected, which may be associated with the alternating vortex shedding from the opposite side edges. If the STROUHAL number is determined by the width of the model St_W, it corresponds well to the St_2 mode: $St_W = f_{0.13} W/U_\infty \approx St_2$.

4.1.3 Description of modal effects with the SPOD

The previous section discussed the complexity of the wake dynamics downstream of the bluff body. Several high-frequency dominant modes are manifested in different regions of the model's wake. The energetic content of these modes is considerably small compared to the energy of the bi-stability.

Conditional averaging delivers insufficient results for these modes due to their lower energy content and spatially dispersed occurrence as listed in Table 2. Therefore, the SPOD is applied to the velocity data to obtain a better identification of the main dynamic features within the wake and their spatial occurrence.

Figure 7a illustrates the temporal evolution of the SPOD coefficient a_i of the wake modes identified in Sect. 4.1.2. The evolution of the SPOD coefficient of the bi-stability (St_0) follows the same trend as observed for the velocity signals in Fig. 3b. The distinct shift between two stable positions is detectable. Phase-averaged velocity fields of the related mode pairs are visualized in Fig. 7b. The contour visualizes the vorticity ω_y. The streamlines visualize the superposition of mean flow and SPOD mode. The spatial characteristics of the computed phase-averaged bi-stability agree well with the velocity fields determined by conditional averaging in Fig. 5. The vortex that dominates the recirculation area dwells half a period on one stable position and shifts after a unpredictable time period to the other stable positions. The calculated energy content of the bi-stability of $K = 22.9\%$ is an order of magnitude larger than the content of the higher frequency modes ($K(St_1) = 1.5\%$), which emphasizes the gap between the bi-stability and the subsequent modes as well as the difficulty for conditional averaging.

The temporal evolution of the SPOD mode coefficients of the dominant coherent structures at the higher frequencies of St_1–St_3 are also plotted in Fig. 7a. The temporal
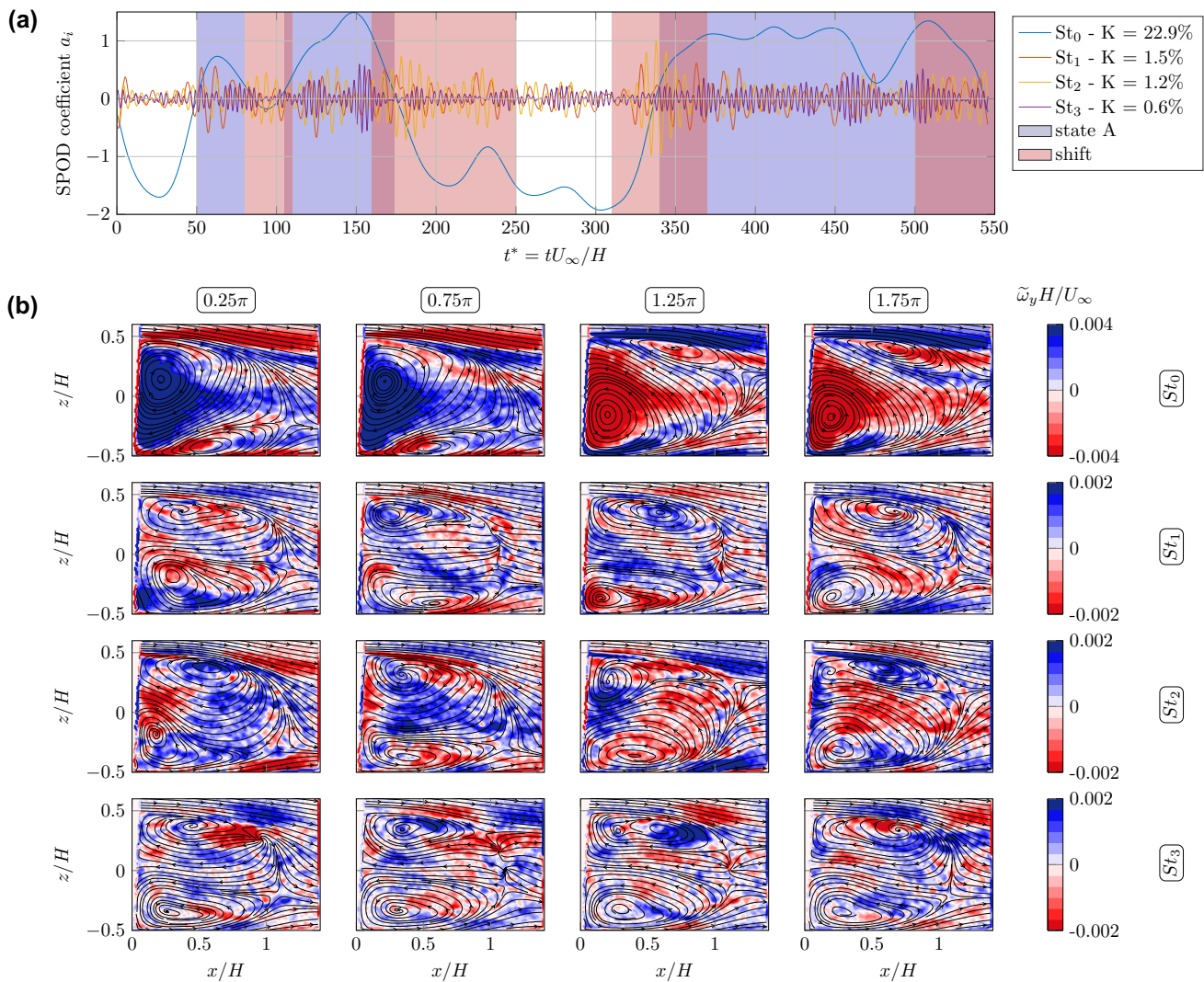
(a)

(b)

Fig. 7 Results of the spectral POD: **a** time evolution of the SPOD mode coefficients a_i for the wake modes $St_0 - St_3$ and **b** visualization of the respective spatial modes during one period in terms of the phase-averaged vorticity $\widetilde{\omega}_y$

behaviors of these modes are linked to the bi-stability. The SPOD mode coefficient of the St_2 mode becomes evident when the flow shifts from one stable position to the other. Otherwise, the oscillation is dampened when the flow dwells in one of the bistable positions. This effect indicates that the dominant wake mode at $St_2 = 0.18$ mainly occurs for a stabilized, toroidal recirculation vortex that is surrounded by similar shear layers. The shear layer mode at a frequency of $St_3 = 0.28$ becomes evident when state A occurs. This indicates that the upper shear layer roll-up is linked to the dominant horseshoe vortex system of state A. The temporal coefficient at the frequency of $St_1 = 0.08$ exhibits a random behavior with a barely noticeable trend to state A. Based on these observations, the SPOD is applied on the modified signals composed of segments highlighted in Fig. 7a. The SPOD for the St_2 mode is computed for measurement

segments which represent a shift from one bistable state to the other. The phase-averaged velocity fields of the St_3 mode are calculated for state A only. The St_1 mode velocity fields are calculated over the entire measurement signal. The obtained phase-averaged velocity fields obtained from the time-segmented velocity field data are visualized in Fig. 7b.

The so-called wake pumping mode at a frequency of $St_1 = 0.08$ exhibits a weak in-phase growth and shrinking of the counter-rotating recirculation vortices, which may be attributed to large regions of inverse vorticity within the recirculation region. It can be speculate about the presence of that wake pumping as described by Duell and George (1999) or Volpe et al. (2015). In contrast to this theory, the extent of the recirculation region does not significantly change during one period and the location of the free stagnation point is nearly unaffected. The phase-averaged SPOD

mode pair at St_2 highlights the alternating vortex shedding as reported in the literature. Initially, the mode's shear layer vorticity has the same orientation, which indicates the alternation of the shear layer effects. As a consequence, the free stagnation point performs obvious vertical oscillations which are linked to the size of the recirculation vortices. This vertical oscillation is also detected in the spectra of Fig. 3d. The presence of the vertical fluctuations downstream of the free stagnation point as mentioned by Khalighi et al. (2012) is also detectable. The phase-averaged flow fields of the SPOD mode at $St = 0.28$ show a variation of the streamwise extent of the upper recirculation vortex. This effect is attributed to an alternating inward and outward deflection of the upper shear layer affected by downstream convecting vortices. Most of the recirculation area and the lower shear layer remain largely unaffected by this mode. An opposite effect at the lower shear layer may be dampened due to the ground effect. However, the entire mode may correspond to the alternating shear layer separation from the opposite base edges, which was first described by Duell and George (1999). Another explanation may be the separation of vorticity from the upper, lateral part of the horseshoe vortex of state A visualized in Fig. 5.

In summary, the SPOD enables an educated insight into the wake dynamics past the GETS model. The link between the bi-stability and the subordinate wake modes could be confirmed. It is noteworthy that the strength of a certain coherent effect (the St_2 mode in this case) is linked to a higher order dominant effect. This may be relevant for the application of flow control intending the suppression of that dominant effect, as often demonstrated for the bi-stability. The achievable drag reduction may be reduced by an intensification of another mode as observed by Li et al. (2016).

4.2 Global effects of flow control

The mean drag and base pressure coefficients (C_D and C_P), and the maximal proliferation of the recirculation area x_R/H are listed in Table 3 for the parameters investigated in the current study. As described by Schmidt et al. (2015), the size of the recirculation area is closely related to the rear base pressure for the applied flow control method. A considerable drag reduction is achievable for small flap angles ($\delta \leq 15°$) without AFC, which is attributed to the boat tailing effect that deflects the freestream onto the flaps. The attached flow affects the pressure recovery over the flaps. The flow completely separates at the base edges of the model when the flap angle increases beyond $\delta = 15°$. For large flap angles, the shear layers are unaffected by the presence of the base flaps, which induces typical baseline wake dynamics and results in similar mean characteristics. The potential benefits of small flap angles for AFC are limited, whereas larger flap angles require an inefficient level of actuation to be effective.

For these flap angles, the mean flow field observations of Schmidt et al. (2015) suggest no significant changes beyond a certain actuation level that is evidently the most effective.

Table 3 Characteristic mean values with and without flow control

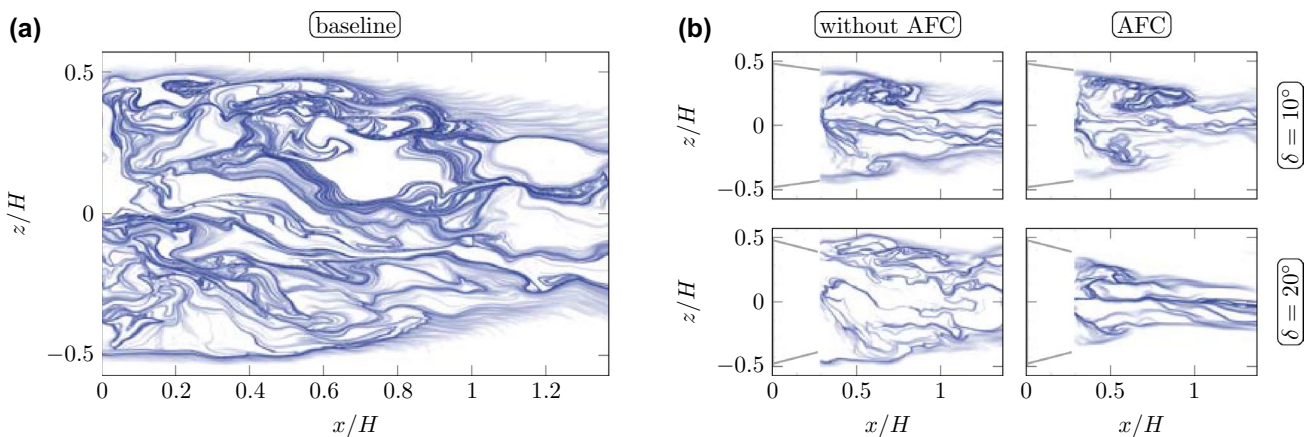|	Baseline	$\delta = 10°$		$\delta = 20°$	
		$C_\mu = 0\%$	$C_\mu = 1.0\%$ ($St_H = 17.0$)	$C_\mu = 0\%$	$C_\mu = 2.5\%$ ($St_H = 24.4$)
C_D	0.35	0.29	0.28	0.34	0.29
$\overline{C_P}$	− 0.36	− 0.23	− 0.21	− 0.3	− 0.09
x_R/H	1 .32	1.23	1.20	1.29	0.88

Fig. 8 Representative FTLE fields of: **a** the baseline configuration, and **b** for the different flow control configurations

Therefore, the selected momentum coefficients represent the most effective C_μ for the respective flap angles in terms of the net drag improvement (Schmidt et al. 2015). Figure 8 presents the distribution of the finite-time LYAPUNOV exponent (FTLE) for the baseline configuration and the investigated flow control configuration. The FTLE is commonly used to visualize the trajectories of particles close to each other over a finite-timespan. In the context of this paper, it is solely used to depict a representative visualization of the instantaneous flow field for the examined configurations. Dark lines indicate a high convergence of neighboring particles (backward time FTLE). The FTLE field of the baseline configuration (Fig. 8a) is dominated by the typical shear layer vortex roll-up downstream of the flow separation. These vortices convect downstream without a significant decrease of their spatial expansion. A disordered occurrence of vortices of the same expansion is detectable within the recirculation area, which indicates that the dominant flow structures have a similar intensity within the entire wake.

The FTLE fields of the flow control configurations visualized in Fig. 8b exhibit various flow characteristics. The flaps deflected at 10° with and without AFC yield similar flow fields, which may be attributed to the minor actuation intensity required to achieve the optimal AFC configuration. The inward deflected shear layer vortices exhibit similar spatial expansion as detected for the baseline configuration, whereas the internal wake appears less turbulent. The influence of the ground is clearly visible for both configurations. For base flaps deflected at 20° without AFC, shear layer conditions are observed to be similar to the baseline configuration due to the flow separation at the base edge. However, a reduction of the vortex extent within the recirculation is noticeable. The flow structures become more organized and symmetric when actuation is applied to the 20° deflected flaps with a momentum coefficient of $C_\mu = 2.5\%$. The flow is deflected onto the base flaps, which significantly decreases the wake size. Furthermore, the wake appears narrower and less turbulent.

4.3 Flow dynamics of flow control

The current section addresses the transient effects of passive flow control via base flaps as well as the combination with active flow control by fluidic oscillators. The respective flow control settings are summarized in Table 3.

Based on the previous descriptions of Sect. 4.2, the flow past the GETS model can be categorized into three different flow states: (1) separated freestream with a damping of the baseline modes due to the presence of the base flaps ($\delta = 20°$, $C_\mu = 0\%$), (2) re-attachment on the minor deflected base flaps without or with minor actuation intensity ($\delta = 10°$, $C_\mu = 0\%$ and 1.0%), and (3) the suppression of most of the typical wake modes by the additional ejection
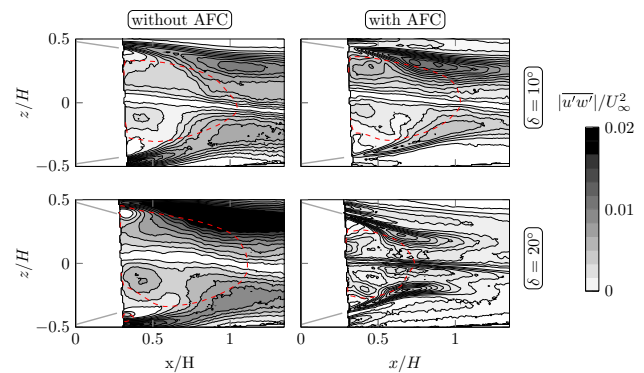

Fig. 9 Distribution of the normalized REYNOLDS shear stresses for the examined flow control configurations. The dashed line illustrates the region of the recirculation ($\overline{u} < 0 m/s$)

of higher momentum required to deflect the flow onto the steeper flaps ($\delta = 20°$, $C_\mu = 2.5\%$). As shown in Tab. 3, the respective oscillation frequencies are about two orders of magnitude larger than the typical wake modes described in Sect. 4.1.2.

Figure 9 visualizes the normalized velocity covariance $|\overline{u'w'}|/U_\infty$ for the selected flow control configurations. Compared to the baseline configuration illustrated in Fig. 3a, a general reduction of the REYNOLDS stresses is noticeable within the recirculation area. This effect may be attributed to the presence of the flaps. The shear layer vortices enhance the interaction between the outer flow and the recirculation zone, thereby injecting additional momentum into the wake. A downstream delay of this mixing procedure away from the model's base leads to an increase in base pressure (Table 3). The wake structures as visualized by the FTLE fields of Fig. 8a are related to the superimposition of the dominant wake modes described in Sect. 4.1. Figure 8b demonstrates the reduced intensity of the coherent structures within the recirculation region, which agrees well with the REYNOLDS stresses (Fig. 9). The configuration with base flaps at $\delta = 20°$ without AFC exhibits high levels of turbulent fluctuation within the shear layers, which is consistent with the baseline configuration shown in Fig. 3a. The size of the recirculation area (dashed line) has a similar extend. A significant reduction of the REYNOLDS stresses is observed for the flow states (2) and (3) at which the flow (re-)attaches onto the base flaps. A further reduction in turbulence intensity is obtained when AFC is enabled. The required momentum ejected by the oscillators increases with flap angle (Schmidt et al. 2015). Hence, the additional input of momentum affects the shear layers farther downstream and increases the symmetry between upper and lower shear layers. A further inward deflection of the flow is achieved by the larger flap angle, which results in a decrease in REYNOLDS stresses.

The vertical base pressure gradient $\delta C_P/\delta z$ of the $\delta = 20°$, $C_\mu = 0\%$ configuration exhibits a vertical switching
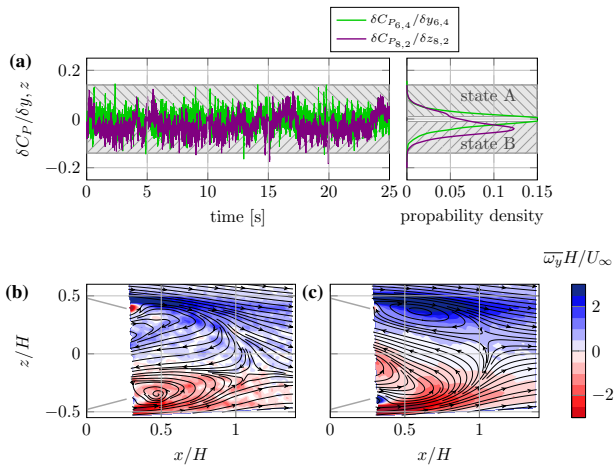
Fig. 10 Conditionally averaged flow fields for $\delta = 20°$, $C_\mu = 0\%$: **a** Time evolution and histograms of the vertical and horizontal pressure gradient on the base, and the distribution of vorticity at **b** state A and **c** state B
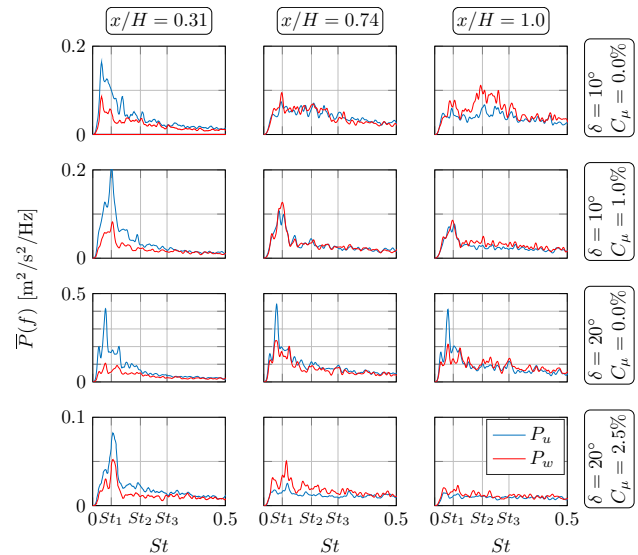

Fig. 11 Power spectral density of the in-plane velocity fluctuations averaged in the vertical direction at: **a** $x/H = 0.31$, **b** $x/H = 0.74$, and **c** $x/H = 1.0$

motion (Fig. 10a) that is similar to the baseline configuration without any flaps (Figs. 4, 5). In addition, the horizontal pressure gradient remains unaffected. This indicates that the bi-stability is also evident when flaps are attached. However, this behavior is significantly dampened. The reduced footprint may be attributed to the downstream shift of the shear layer mixing and the larger distance to the pressure sensors. Again, conditional averaging based on the vertical pressure gradient is attempted and visualized in Fig. 10. State B is represented by 68% of the PIV snapshots, whereas state A is underrepresented by 16% of the recorded images. However, the main formation of the vortex system is observed. The alternating dominance of one of the recirculation vortices is similar to the bistable flow effect of the baseline configuration. The dominant part of the recirculation extents upstream into the cavity. The outer flow circulates around the respective flap's trailing edge and feeds the dominant structure. Evrard et al. (2016) obtained a stabilization of the wake for normalized flap lengths larger than $l_{flap}/H \approx 0.24$ for a bluff body with an aspect ratio of $H/W = 0.85$. According to the inverse orientation of the bi-stability in this study, the associated reference length for the comparison is the width of the GETS model W. The normalized cavity size of the model is $l_{flap}/W \approx 0.34$, which is larger than determined by Evrard et al. (2016). The presence of the bi-stability for that flap length may be attributed to the large flap deflection angle δ and the step between trailing edge and flap, as shown in Fig. 1a. This particular design may facilitate the development of baseline shear layers which are less affected by the flaps.

Figure 11 visualizes the integrated power spectral density ($\overline{P}$) along the z-coordinate at different streamwise positions as calculated in Fig. 6b. A lower frequency mode at

a STROUHAL number of $St \approx 0.06 - 0.07$ occurs when the actuation is disabled with increasing intensity farther downstream. However, this frequency may also be attributed to the wake pumping/shear layer effect described by Duell and George (1999). The shift to lower frequencies may be attributed to a partial suppression of the interaction between recirculation area and the separated shear layer vortices. The St_2 and St_3 modes are detectable for the passive flow control configurations but play an inferior role in terms of the total power. For the active flow control configurations, the St_2 and St_3 modes mostly disappear. The St_1 mode is clearly detectable for the configurations with enabled AFC, whereas the entire frequency band is significantly dampened for the higher momentum coefficient of $C_\mu = 2.5\%$. This behavior summarizes the impact that AFC has on the bluff body wake dynamics. The additional momentum of the AFC deflects the flow onto the flaps which diverts the direction of the shear layers inward and inhibits the alternating vortex shedding. The presence of the St_1 mode as the predominantly detectable wake mode for the AFC configurations motivates further investigations regarding its spatial characteristics. Therefore, the SPOD is applied to the AFC configurations to determine the phase-averaged velocity fields of the respective SPOD mode pair. Figure 12 visualizes the phase-averaged velocity fields of the related SPOD mode for both AFC configurations. The relative energy of the St_1-SPOD mode at a flap angle of $\delta = 10°$ and $C_\mu = 1.0\%$ is $K = 5.69\%$ and decreases to $K = 2.02\%$ for $\delta = 20°$, $C_\mu = 2.5\%$. The relative increase in energy K compared to the baseline configuration is attributed to the absence of the bi-stability. The applied momentum at a flap angle of $\delta = 10°$ cannot suppress the asymmetry
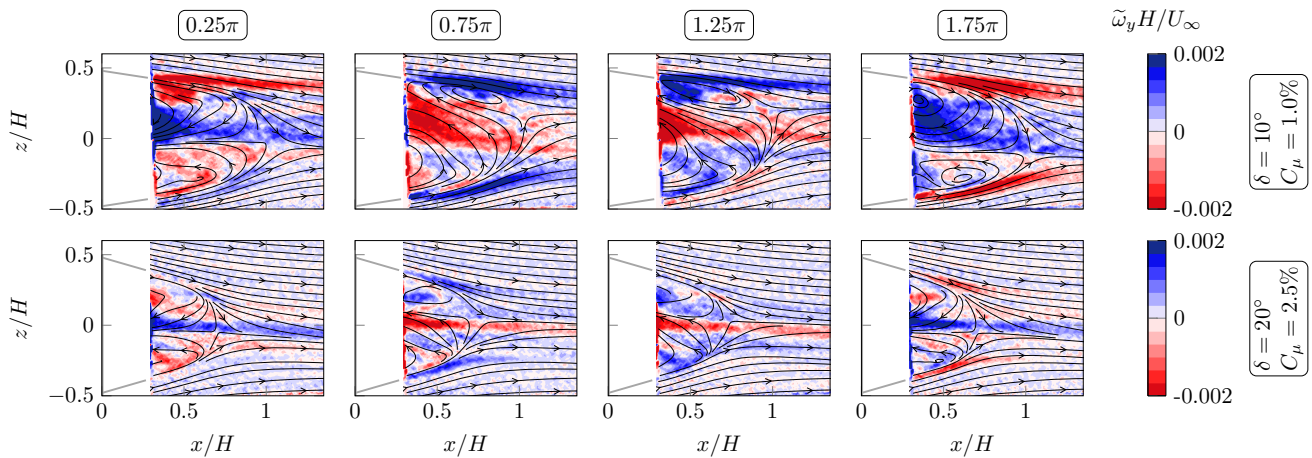
Fig. 12 Temporal evolution of the phase-averaged vorticity $\widetilde{\omega}_y$ of the St_1 mode of the active flow control configurations

due to the ground effect. The larger momentum coefficient of $C_\mu = 2.5\%$ at the 20° deflected flaps balances the upper and lower shear layers, as observed in Fig. 9. A vertical shift of the free stagnation point is detectable for $\delta = 10°$, which remains at a nearly constant location for $\delta = 20°$. However, the general dynamics of the phase-averaged velocity fields reveal similar effects for both flap angles. The vorticity of the opposite shear layers is in phase, whereas the recirculation area as well as the far field are dominated by inverse vorticity. Both modes may be attributed to the same underlying shear layer dynamics.

5 Conclusion

The wake dynamics of a bluff body model equipped with base flaps and fluidic oscillators for drag reduction are examined through wind tunnel experiments. The flow dynamics in the wake of the baseline configuration and for selected passive and active flow control configurations are assessed. Stereoscopic high-speed PIV data and time-resolved pressure measurements are used to perform conditional averaging and spectral analysis. Furthermore, the spectral POD method is employed on the time-resolved velocity data.

The test conditions and the model geometry promote the occurrence of the long-time wake shift between two stable positions, which has been reported in several studies. However, in the current study, the bi-stability occurs in the vertical direction instead of the reported horizontal direction at an AHMED body, which is due to the height of the model being larger than its width. The vertical pressure gradient at the model base is utilized for conditional averaging to illustrate the spatial development of the main vortex systems. The SPOD identified similar trends for the bi-stability.

The spatial development of the high-frequency modes, which are the wake pumping frequency at $St_1 = 0.08$, the shear layer interaction at $St_2 = 0.18$, and the upper shear layer mode at $St_3 = 0.28$, is also visualized. The estimated energy content is an order of magnitude lower than the energy content of the bi-stability. The time evolutions of the SPOD coefficients illustrate a connection to the bi-stability. The St_2 mode occurs when the wake tends to the symmetric position and the St_3 mode is most apparent at bistable state A, whereas the St_1 mode does not show a significant connection to the bi-stability. Phase-averaged flow fields are calculated for the time periods which they become apparent for. The St_1 and St_2 modes affect large regions within the wake, whereas the St_3 represents an upper shear layer mode.

The application of flow control significantly changes the wake dynamics. Large flap angles without AFC lead to flow separation and the occurrence of typical baseline wake modes, however, with a dampened bi-stability mode. Conditional averaging reveals similar bistable flow dynamics as determined for the baseline configuration. The St_2 and St_3 modes are dampened by the presence of the base flaps and disappear when AFC is applied in addition. The St_1 mode occurs for all flow control cases with a minor shift to a lower frequency for the passive flow control. The phase-averaged flow fields for the AFC configurations demonstrate that similar dynamics occur within the respective limitation.

Overall, this study demonstrates that the aerodynamic drag is directly linked to the coherent wake dynamics and their energetic content. Base flaps and active flow control reduce the impact of these structures and increase the rear base pressure. The connection between bluff body drag and the different wake modes may be considered for more effective and efficient flow control approaches.

decomposition. This work is part of the research project "Investigation of the Unsteady Wake behind a Generic Tractor-Trailer with Different Boundary Conditions" (PA 920/26-1). The authors would like to thank the German Research Foundation (DFG) for its financial support.

References

Ahmed SR, Ramm G, Faltin G (1984) Some salient features of the time-averaged ground vehicle wake. SAE Technical Paper (840300). https://doi.org/10.4271/840300

Barros D, Ruiz T, Borée J, Noack BR (2014) Control of a three-dimensional blunt body wake using low and high frequency pulsed jets. Int J Flow Control 6(1):61–74. https://doi.org/10.1260/1756-8250.6.1.61

Barros D, BorTe J, Noack BR, Spohn A (2016a) Resonances in the forced turbulent wake past a 3D blunt body. Phys Fluids 28(6):065,104. https://doi.org/10.1063/1.4953176

Barros D, BorTe J, Noack BR, Spohn A, Ruiz T (2016b) Bluff body drag manipulation using pulsed jets and Coanda effect. J Fluid Mech 805:422–459. https://doi.org/10.1017/jfm.2016.508

Barros D, BorTe J, Cadot O, Spohn A, Noack BR (2017) Forcing symmetry exchanges and flow reversals in turbulent wakes. J Fluid Mech 829:R1. https://doi.org/10.1017/jfm.2017.590

Brackston RD, Garcia de la Cruz JM, Wynn A, Rigas G, Morrison JF (2016) Stochastic modelling and feedback control of bistability in a turbulent bluff body wake. J Fluid Mech 802:726–749. https://doi.org/10.1017/jfm.2016.495

Cadot O, Evrard A, Pastur L (2015) Imperfect supercritical bifurcation in a three-dimensional turbulent wake. Phys Rev E 91(063):005. https://doi.org/10.1103/PhysRevE.91.063005

Cooper KR (1985) The Effect of Front-Edge Rounding and Rear-Edge Shaping on the Aerodynamic Drag of Bluff Vehicles in Ground Proximity. SAE Technical Paper (850288). https://doi.org/10.4271/850288

Duell E, George A (1999) Experimental study of a ground vehicle body unsteady near wake. SAE Technical Paper (1999-01-0812). https://doi.org/10.4271/1999-01-0812

Englar RJ (2001) Advanced aerodynamic devices to improve the performance. SAE Technical Paper, Economics, Handling and Safety of Heavy Vehicles. https://doi.org/10.4271/2001-01-2072

Evrard A, Cadot O, Herbert V, Ricot D, Vigneron R, Délery J (2016) Fluid force and symmetry breaking modes of a 3D bluff body with a base cavity. J Fluid Struct 61:99–114. https://doi.org/10.1016/j.jfluidstructs.2015.12.001

Garcia D (2011) A fast all-in-one method for automated post-processing of PIV data. Exp Fluids 50(5):1247–1259. https://doi.org/10.1007/s00348-010-0985-y

Grandemange M, Gohlke M, Cadot O (2013a) Bi-stability in the turbulent wake past parallelepiped bodies with various aspect ratios and wall effects. Phys Fluids 25(9):095,103. https://doi.org/10.1063/1.4820372

Grandemange M, Gohlke M, Cadot O (2013b) Turbulent wake past a three-dimensional blunt body. Part 1. Global modes and bi-stability. J Fluid Mech 722:51–84. https://doi.org/10.1017/jfm.2013.83

Grandemange M, Gohlke M, Cadot O (2014) Turbulent wake past a three-dimensional blunt body. Part 2. Experimental sensitivity analysis. J Fluid Mech 752:439–461. https://doi.org/10.1017/jfm.2014.345

Khalighi B, Zhang S, Koromilas C, Balkanyi S, Bernal LP, Iaccarino G, Moin P (2001) Experimental and computational study of unsteady wake flow behind a bluff body with a drag reduction device. SAE Technical Paper (2001-01-1042). https://doi.org/10.4271/2001-01-1042

Khalighi B, Chen KH, Iaccarino G (2012) Unsteady aerodynamic flow investigation around a simplified square-back road vehicle with drag reduction devices. J Fluids Eng 134(6):061,101. https://doi.org/10.1115/1.4006643

Krajnović S, Davidson L (2003) Numerical study of the flow around a bus-shaped body. J Fluids Eng 125(3):500–509. https://doi.org/10.1115/1.1567305

Li R, Barros D, Borée J, Cadot O, Noack BR, Cordier L (2016) Feedback control of bimodal wake dynamics. Exp Fluids 57(10):158. https://doi.org/10.1007/s00348-016-2245-2

Lucas JM, Cadot O, Herbert V, Parpais S, Dtlery J, (2017) A numerical investigation of the asymmetric wake mode of a squareback Ahmed body–effect of a base cavity. J Fluid Mech 831:675–697. https://doi.org/10.1017/jfm.2017.654.

Mason WT, Beebe PS (1978) The drag related flow field characteristics of trucks and buses. In: Aerodynamic drag mechanisms of bluff bodies and road vehicles, Springer, New York, pp 45–93. https://doi.org/10.1007/978-1-4684-8434-2_3

Pavia G, Passmore M, Sardu C (2017) Evolution of the bi-stable wake of a square-back automotive shape. Exp Fluids 59(1):20. https://doi.org/10.1007/s00348-017-2473-0

Perry AK, Pavia G, Passmore M (2016) Influence of short rear end tapers on the wake of a simplified square-back vehicle: wake topology and rear drag. Exp Fluids 57(11):169. https://doi.org/10.1007/s00348-016-2260-3

Peterson RL (1981) Drag reduction obtained by the addition of a boat-tail to a box shaped vehicle. NASA Contractor Report 163113

Schmidt HJ, Woszidlo R, Nayeri CN, Paschereit CO (2015) Drag reduction on a rectangular bluff body with base flaps and fluidic oscillators. Exp Fluids 56(7):151. https://doi.org/10.1007/s00348-015-2018-3

Sieber M, Paschereit CO, Oberleithner K (2016a) Advanced Identification of Coherent Structures in Swirl-Stabilized Combustors. ASME J Eng Gas Turbines Power. https://doi.org/10.1115/1.4034261

Sieber M, Paschereit CO, Oberleithner K (2016b) Spectral proper orthogonal decomposition. J Fluid Mech 792:798–828. https://doi.org/10.1017/jfm.2016.103

Van Raemdonck GMR, Van Tooren MJL (2008) Time-averaged phenomenological investigation of a wake behind a bluff body. In: Proceedings of bluff bodies aerodynamics and applications VI international colloquium

Volpe R, Devinant P, Kourta A (2015) Experimental characterization of the unsteady natural wake of the full-scale square back Ahmed body: flow bi-stability and spectral analysis. Exp Fluids 56(5):99. https://doi.org/10.1007/s00348-015-1972-0

Woszidlo R, Wygnanski IJ (2011) Parameters governing separation control with sweeping jet actuators. In: AIAA 2011, 29th AIAA Applied Aerodynamics Conference. https://doi.org/10.2514/6.2011-3172

Woszidlo R, Ostermann F, Nayeri CN, Paschereit CO (2015) The time-resolved natural flow field of a fluidic oscillator. Exp Fluids 56(6):125. https://doi.org/10.1007/s00348-015-1993-8